THE JOURNAL OF PHYSICAL CHEMISTRY C

pubs.acs.org/JPCC

Article

CO_2 Capture by Nickel Hydroxide Interstratified in the Nanolayered Space of a Synthetic Clay Mineral

Kristoffer W. Bø Hunvik, Patrick Loch, Leide P. Cavalcanti, Konstanse Kvalem Seljelid, Paul Monceyron Røren, Svemir Rudić, Dirk Wallacher, Alexsandro Kirch, Kenneth Dahl Knudsen, Caetano Rodrigues Miranda, Josef Breu,* Heloisa N. Bordallo,* and Jon Otto Fossum*

Cite This: *J. Phys. Chem. C* 2020, 124, 26222−26231

Read Online

ACCESS | Metrics & More | Article Recommendations | Supporting Information

ABSTRACT: Clay minerals can adsorb large amounts of CO_2 and are present in anthropogenic storage sites for CO_2. Nanoscale functionalization of smectite clay minerals is essential for developing technologies for carbon sequestration based on these materials and for safe-guarding relevant long-term carbon storage sites. We investigate the adsorption mechanisms of CO_2 in dried and hydrated synthetic Ni-exchanged fluorohectorite clay—using a combination of powder X-ray diffraction, Raman spectroscopy, and inelastic neutron scattering. Both dried and hydrated Ni-exchanged fluorohectorite show crystalline swelling and spectroscopic changes in response to CO_2 exposure. These changes can be attributed to interactions with $[Ni(OH)_{0.83}(H_2O)_{1.17}]_{0.37}^{1.17+}$-interlayer species, and swelling occurs solely in the interlayers where this condensed species is present. The experimental conclusions are supported by density functional theory simulations. This work demonstrates a hitherto overlooked important mechanism, where a hydrogenous species present in the nanospace of a clay mineral creates sorption sites for CO_2.

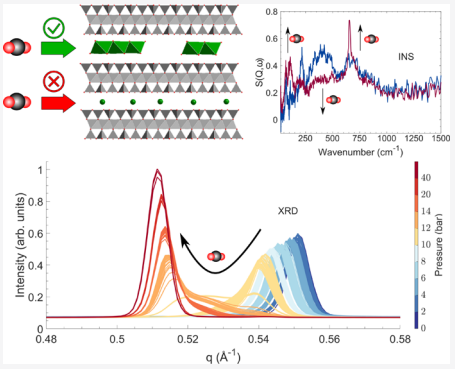

Continuous and increasing release of greenhouse gases, in particular CO_2, to the atmosphere has a detrimental impact on our environment. In addition to emission reduction, it is imperative to establish effective ways of capturing these gases. Clay minerals have become an attractive alternative for investigating CO_2 capture because of their excellent behavior in adsorption and catalysis.[1] This is in addition to their abundance and stability, which make them potentially scalable for industrial processes.

Smectite clay minerals, such as hectorite and montmorillonite, are known to readily swell in response to water,[2−4] CO_2[5−10] and organic compounds.[11,12] They consist of two-dimensional nanolayered stacks possessing a negative layer charge due to nonequivalent substitutions of atoms in the layers. The negative layer charge is typically counterbalanced by exchangeable interlayer cations, for example Na^+, Ca^{2+}, and K^+.

The sorption of CO_2 in smectite clays at various hydration states as well as under gaseous and supercritical CO_2 conditions has been studied by a wide range of techniques, such as X-ray and neutron diffraction, infrared spectroscopy, nuclear magnetic resonance, quartz crystal microbalance, and volumetric/gravimetric gas adsorption.[5−7,13−21] The sorption of CO_2 in smectite clays has been shown to largely depend on the initial hydration, the interlayer cation, and the specific clay type. For montmorillonite (Mt) and OH-hectorite (Hec), experiments and simulations at 323 K and 90 bar have shown that for smaller interlayer cations with a high hydration energy (e.g. Na^+, Ca^{2+}, and Mg^{2+}), a submonolayer of water is necessary to open up the interlayer to swell in response to CO_2.[8−10] However, for larger interlayer cations with low hydration energy (e.g. Cs^+, K^+, and NH_4^+), CO_2 is intercalated even in the absence of water.[8−10]

Natural Hec has a varying composition of F^- and OH^- groups, whereas fluorohectorite is a synthetic Hec with only fluorine groups. Simulations[22] have shown that by varying the $F^-/(F^- + OH^-)$ composition, the $CO_2/(CO_2 + H_2O)$ ratio increases with increasing F^- substitution. It has previously been demonstrated that a fluorinated Hec exchanged with Na^+, Li^+, and Ni^{2+} swells in response to CO_2 exposure[5,6] and that Ni-Hec showed a much larger adsorption of CO_2 than Li-Hec and Na-Hec.[7]

Here, we report a hitherto overlooked mechanism for CO_2 sorption in Ni-Hec as studied with synchtrotron X-ray diffraction, Raman spectroscopy, and inelastic neutron scattering (INS). The intercalation properties of Ni^{2+} in smectites have been shown to be substantially different from

Received: August 6, 2020
Revised: October 27, 2020
Published: November 16, 2020

other interlayer cations.[6,23] As recently reported in Loch et al.,[24] Ni-Hec forms an ordered interstratification with a chlorite-like condensed $[Ni(OH)_{0.83}(H_2O)_{1.17}]_{0.37}^{1.17+}$ species in one interlayer and a smectite-like structure with hydrated Ni^{2+} cations in the adjacent interlayer. By employing powder X-ray diffraction (PXRD), we investigate the structural changes in response to CO_2. We utilize *in situ* Raman scattering combined with PXRD, which allows studying how CO_2 adsorption changes the local structure. INS has no selection rules for the vibrational modes and a large cross section of the hydrogen atoms, making the signal from the water motions and other hydrogenous species, such as nickel hydroxide, prominent.[25] INS has previously been successfully employed to study how layer charge and cations influence the hydration properties of saponite, montmorillonite, and beidelitte.[26,27]

By combining PXRD, Raman spectroscopy, and INS, we elucidate the active mechanisms of CO_2 sorption for Ni-Hec in the dried (at 150 °C under dynamic vacuum) and hydrated (equilibrated at 43% r.h.) states. To support our experimental conclusions, we have performed density functional theory calculations (DFT).

METHODS

Materials. Na-Hec with a stoichiometric composition of $Na(Mg_5Li)Si_8O_{20}F_4$ was prepared via melt synthesis according to a published procedure,[2] followed by annealing (6 weeks, 1045 °C) to improve charge homogeneity and phase purity.[28] Ni-Hec was prepared by cation exchange of Na-Hec with 0.2 M nickel−acetate solution (>10 fold excess of the CEC, 5 times). The exchanged Ni-Hec was washed 5 times with Millipore water. The hydration and drying procedures are described below for each type of experiment.

***In Situ* Powder X-ray Diffraction and *In Situ* Raman Spectroscopy.** For Ni-Hec, combined Raman and synchrotron X-ray powder diffraction data were collected at the Swiss-Norwegian Beamlines (SNBL, station BM01B) at ESRF, Grenoble, France. PXRD data were measured at a wavelength of 0.77495 Å using a 2D PILATUS2M detector.[29] The 2D diffractograms were integrated using the SNBL Bubble software to provide rebinned 1D diffraction patterns. The powdered samples were contained in borosilicate capillaries mounted in a custom made high-pressure sample cell based on the design by Jensen et al.[30] The temperature of the capillary was controlled by an Oxford Cryostream 700+ nitrogen blower. The cell was connected to a gas handling system providing vacuum (10^{-6} mbar) from a turbomolecular pump or pressurized CO_2 of quality 99.9995%. The dried Ni-Hec sample was prepared at 150 °C in the capillary sample cell for ∼2 h and was considered sufficiently dried since the (00*l*) Bragg reflections did not change position after reducing the temperature to 300 K. The hydrated sample was prepared in a desiccator prior to the measurements corresponding to 2 WL hydration. Raman spectra were collected on a Renishaw RA 100 Raman analyzer, using a 532 nm (green) excitation wavelength in backscattering mode. Spectra were recorded in the range 100−4000 cm^{-1} with a step size 1.2 cm^{-1}, and 5 scans per spectrum were recorded with an exposure of 60 s.

Included in the Supporting Information are PXRD data on a dried Na-Hec as a reference.

Inelastic Neutron Scattering. Inelastic neutron spectra were recorded using the TOSCA spectrometer[31−33] at the ISIS facility, Rutherford Appleton Laboratory, UK. TOSCA is an indirect geometry time-of-flight spectrometer spanning an energy-transfer range up to 4000 cm^{-1} in neutron energy loss (E_T) with a spectral resolution of 1.25% E_T.[31] In order to minimize thermal effects, the spectra were recorded at $T < 20$ K.

Ni-Hec both in the hydrated and dried state was prepared for the INS experiment. Hydrated samples were equilibrated for 5 days at 43% relative humidity in a desiccator with saturated K_2CO_3 solution, while dried samples were prepared by heating the samples to 145 ± 15 °C under high vacuum (10^{-6} mbar) for 18 h (Ni-Hec sample). As a reference, included in the Supporting Information are data on dried Na-Hec (7 h at 145 ± 15 °C under high vacuum) with the same experimental procedure as dried Ni-Hec.

The samples were placed in an aluminum foil sachet and mounted in stainless steel cylinders. The sample holder was then mounted on a center stick connected to a gas handling system. Prior to measurements, the cell was leak tested with 50 bar helium which was pumped away in the case of dried samples and leaked slowly to atmospheric pressure in the case of the hydrated samples.

Dried Ni-Hec was measured under vacuum, at 5 bar of CO_2, 44 bar of CO_2, and after releasing CO_2 (∼ 24 h under vacuum). The hydrated sample was measured at ambient pressure and 44 bar CO_2 pressure. Each pressure step was achieved by heating up the sample holder and center stick to room temperature, exposing the sample to CO_2 grade 99.9995% for 20 min, and subsequently cooling down to $T < 20$ K with CO_2 still inside the sample holder. Each INS measurement lasted around 6−8 h, depending on the amount of hydrogen in the sample.

The data were reduced using the software package Mantid.[34] After subtracting the signal from the empty cell, the spectra were scaled by the sample mass. After exposure to CO_2, the signal was normalized to have the same area under the curve as the initial spectrum.

DFT Simulations. We performed *ab initio* investigations based on density functional theory calculations[35,36] considering the generalized gradient approximation with the state-of-the-art van der Waals-corrected density functional developed by Berland and Hyldgaard,[37] as implemented in the Siesta package.[38] Norm-conserving pseudopotentials were used with double-zeta plus polarization and spin-polarized localized atomic orbital basis sets considering an energy cutoff of 400 Ry. The crystallographic structure reported by Breu et al.[39] was used for the Ni-Hec model with the unit cell containing 39 atoms. For β-$Ni(OH)_2$, we took the structural model from the Aflowlib repository.[40] Adsorbents were allowed to relax during structural optimization using the conjugate gradient method under the self-consistent cycles considering a criteria of 0.01 eV/Å for the force minimization. The adsorption energy E_{Ads} was calculated following the equation

$$E_{Ads} = E_{Total} - E_{Crystal} - E_{Molecule} \quad (1)$$

where E_{Total} is the total energy for the adsorbed molecule in the most favorable adhesion site; $E_{Crystal}$ and $E_{Molecule}$ are the total energies for the isolated systems.

RESULTS AND DISCUSSION

Powder X-ray Diffraction. *Dried Ni-Hec.* In Figure 1, the swelling of Ni-Hec at 300 K with increasing CO_2 pressure is shown. After drying the sample in vacuum at 150 °C, an intense Bragg reflection is observed at 0.551 $Å^{-1}$, corresponding to a d-value of 11.40 Å, which recently was identified as the

https://dx.doi.org/10.1021/acs.jpcc.0c07206
J. Phys. Chem. C 2020, 124, 26222−26231

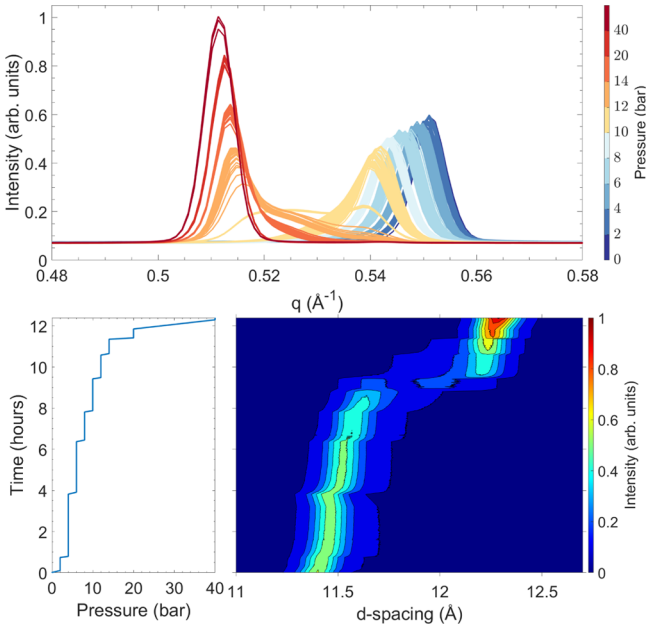

Figure 1. Evolution of the (002) Bragg reflection as a function of pressure at 300 K for dried Ni-Hec. In the top panel, the Bragg reflection is plotted with colors indicating pressure given by the color bar. The bottom left panel is the pressure of CO_2 applied to the sample as a function of time. The bottom right panel depicts a contour plot where the horizontal axis corresponds to *d*-spacing ($d = 2\pi/q$), the vertical axis corresponds to time, and the color represents the intensity.

(002) Bragg reflection of an ordered interstratification of a nonhydrated, collapsed interlayer and a chlorite-type interlayer of $[Ni(OH)_{0.83}(H_2O)_{1.17}]_{0.37}^{1.17+}$.[24]

With increasing pressure of CO_2, transient interstratified domains are observed in addition to initial and final state domains, transferring the weight from one state to the other. Since swelling is an inherent two-dimensional process, reflections gradually move as the number of swollen interlayers increases and thus the weighting of the interstratified stacks becomes larger. For intermediate stages, the intensities are not proportional to the volumes of swollen and not yet swollen interlayers because of the weighting differing from the 1:1 ratio. The nonlinear transition of the educt to product intensities is an artifact that may be attributed to the effect of interstratification.

At pressures above 10 bar, the educt phase starts to vanish, while the product basal spacing continues to be shifted to larger *d*-spacings until around 12 bar, where the swelling reaches a plateau. At the final pressure of 40 bar CO_2, a symmetric peak with a maximum intensity centered at 0.511 Å^{-1} corresponding to a *d*-value of 12.29 Å is observed. As the inspected Bragg reflection is (002), a total interlayer expansion of 1.78 Å is observed. While intermediate reflections, in line with Mering's rules, are broadened due to interstratification, the width of the Bragg reflection is unchanged when comparing the initial state and the final state, indicating completion of swelling. The observed swelling is clearly correlated with the gravimetric adsorption data presented in the Supporting Information, demonstrating that the swelling is caused by uptake of CO_2. As there is limited change above 20 bar, these results also provide valuable information on what could occur in a geological storage where the temperature and pressure can be >40 °C and >90 bar.[41]

Hydrated Ni-Hec. In Figure 2, the expansion upon CO_2 exposure of a Ni-Hec hydrated at 300 K is shown, adopting the

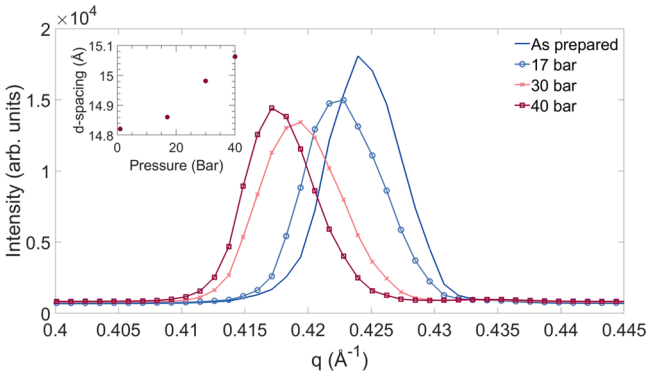

Figure 2. X-ray diffraction pattern of the (002) Bragg reflection for hydrated Ni-Hec at 300 K following the evolution with respect to pressure for the sample as-prepared at 1 bar up to 40 bar of CO_2. The inset shows the corresponding *d*-spacing evolution as a function of pressure.

2 WL hydrate state with a (002) Bragg reflection at 14.82 Å,[24] which gradually increases to 15.06 Å as the CO_2 pressure increases. Compared to the dried sample, a smaller increase is observed, that is 0.48 *versus* 1.78 Å. Again, the width of the Bragg reflection at the initial state and final CO_2 exposed state is comparable.

Interestingly, upon swelling in response to CO_2, the crystallinity was improved by reducing planar defects as indicated by cross-reflections in the region of the 11/02 band gaining significant intensity (Figure 3). While the starting material shows a λ-shaped band typical for turbostratic stacking, after CO_2 saturation, a 3D ordered stacking is observed with a refined unit cell of ($C2/m$, a = 5.2504 Å, b = 9.0780 Å, c = 30.25 Å, β = 96.6280°, α/γ = 90°). Such a disorder/order transformation has previously been observed at the transition from 1 WL to 2 WL hydrate of Na-Hec[4,28] and has been attributed to a strengthened interaction of interlayer species with the surface of the 2:1-silicate layers via hydrogen bonding. In the present case, this disorder/order transformation was reversible and was lost again as the CO_2 pressure was reduced, as shown in Figure S5.

***In Situ* Raman Spectroscopy.** *In situ* Raman spectra corresponding to pristine (not yet exposed to CO_2) hydrated Ni-Hec (Figures 2 and 3) and exposed to 40 bar CO_2 pressure are shown in Figure 4. The assignment of the vibrations is given in Table 1. A very high fluorescent background did not allow us to record Raman spectra for dried Ni-Hec. Fluorescence is commonly observed in clay minerals;[42] however, in this study, fluorescence also arises from the electronic structure of the Ni^{2+} cations, which have a $3d^8$ valence configuration.[43] Local distortion of octahedrally coordinated chlorite-type $[Ni(OH)_{0.83}(H_2O)_{1.17}]_{0.37}^{1.17+}$ greatly affects the associated orbitals also contributing to the observed fluorescence.[43]

Modes associated to the Hec structure are assigned according to Rinaudo et al.[44] As recently shown in Loch et al.,[24] Ni-Hec contains both Ni^{2+} and $[Ni(OH)_{0.83}(H_2O)_{1.17}]_{0.37}^{1.17+}$ species segregated into adjacent interlayers. Thus, the vibrations at 319 cm^{-1} (#4) and 467 cm^{-1} (#7) can be associated to Ni−OH vibrations.[45] We also observe a third feature around 506 cm^{-1} (#8) that can be

https://dx.doi.org/10.1021/acs.jpcc.0c07206
J. Phys. Chem. C 2020, 124, 26222−26231

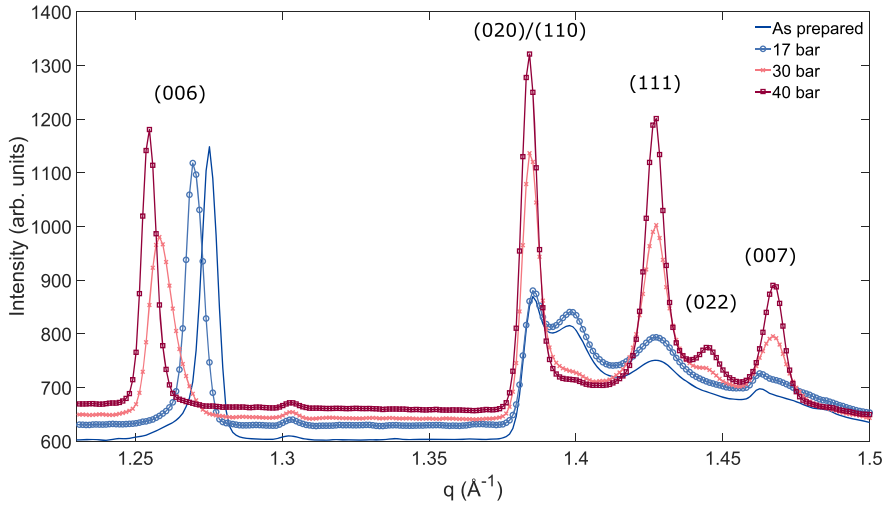

Figure 3. X-ray diffraction pattern of hydrated Ni-Hec as a function of CO_2 pressure at 300 K.

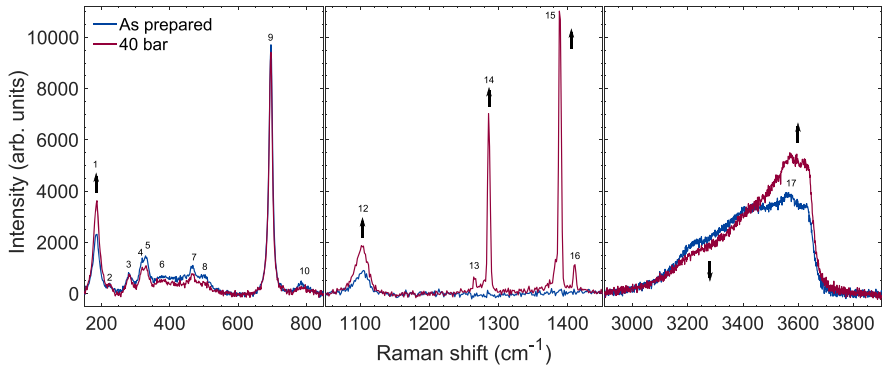

Figure 4. Raman spectra of hydrated Ni-Hec as prepared at 1 bar and exposed to 40 bar of CO_2 at 300 K. Numbering indicates the assigned vibrations, and arrows highlight prominent changes in the spectra. Mode assignment is summarized in Table 1.

Table 1. Raman Vibration Assignment of the Peaks Presented in Figure 4

feature number	position (cm^{-1})	suggested assignment
1	184	Mg,LiO$_6$ octahedra[44]
2	222	(small vibration) unassigned
3	280	O−H−O vibrations[45]
4	319	$A_{1g}(T)$, $E_g(T)$ or $E_g(R)$ Ni-(OH)[45]
5	330	bending SiO$_4$[44]
6	371	stretch Mg−O[50]
7	467	$A_{1g}/E_u(LO)/A_{2u}(LO)$ Ni-(OH)[45]
8	506	$A_{1g}(T)$ or $E_g(T)$ Ni-(OH)[45]
9	696	ν_s SiO$_4$[44]
10	783	vibration SiO$_4$[50]
11	1006	vibration SiO$_4$[50]
12	1105	ν_{as} SiO$_4$[44]
13	1265	CO_2; hot band[51]
14	1286	CO_2; $2\nu_2$[51]
15	1388	CO_2; ν_1[51]
16	1410	CO_2; hot band[51]
17	3565	Ni-(OH) A_{1g} O−H[45]

assigned either to the presence of structural defects and/or to a $E_g(R)$ mode for the Ni−OH structure.

In the range of OH-modes between 3000 and 3600 cm^{-1}, the sharp feature at 3565 cm^{-1} (#17) is assigned to the A_{1g} O−H stretch of Ni−OH.[45] The remaining modes in this region are assigned to water present in the clay. These can be divided into water bonded directly to the interlayer cations, interlayer water that does not directly interact with the cations, and water outside the interlayers.[46] The latter constitutes a tiny amount because of the large aspect ratio of the clay particles,[28] which results in a relatively low external surface area. The water not directly coordinated to the interlayer cations can either be in the chlorite-like or the smectite-like layers. Given these possibilities, an unambiguous assignment of the modes in this region is difficult.

After exposure to 40 bar of CO_2 (Figure 4), the intensity of bands related to CO_2 at 1286 cm^{-1} (#14) and 1388 cm^{-1} (#15) increases. There is also a clear change in the intensity associated to OH-groups between 3000 and 3600 cm^{-1} and an increase of intensity and sharpening of the vibration associated to the Mg, LiO$_6$ octahedra, and the asymmetric stretch of SiO$_4$.

Because the density ratio between intercalated and non-intercalated gaseous CO_2 in the probing volume of the Raman laser is low, the intensity of the CO_2 vibrations is most likely to be dominated by gaseous CO_2 in the capillary. The increase and sharpening of the modes associated to the octahedral and the tetrahedral sheet of the clay layers can be associated to the order−disorder transition observed by PXRD (Figures 2 and 3). Indeed, an increased long-range order in clays is known to enhance the signal to noise-ratio and sharpen the peaks.[47] The shape change in the H_2O/OH-region could indicate some local modification of the water population in the interlayers. In

https://dx.doi.org/10.1021/acs.jpcc.0c07206
J. Phys. Chem. C 2020, 124, 26222−26231

addition, there are clear changes for the OH-stretching bands. The observed changes for the OH-stretching vibrations bear resemblance to previously observed changes when β-$Ni(OH)_2$ transforms to α-$Ni(OH)_2$,[48] which indicates that CO_2 has an effect on the intercalated $[Ni(OH)_{0.83}(H_2O)_{1.17}]_{0.37}^{1.17+}$ species. The observed increase of intensity around 1100 cm^{-1} (#12) can then, in addition to ordering of the clay crystal structure, be associated with introduced stress in the nickel hydroxide lattice.[48] The increased intensity at 1100 cm^{-1} (#12) could also be due to carbonate (CO_3^{2-}), which is known to form a strong symmetric stretch ν_1 mode in this region for Raman spectroscopy.[49] The remaining modes for carbonate, which would be located around 880, 1400, and 680 cm^{-1}, are weaker[49] and, in this case, located in regions where other modes due to the clay and CO_2 gas phase are dominating.

Inelastic Neutron Spectroscopy. INS spectra of pristine Ni-Hec, both in dried and equilibrated at 43% r.h. states, are presented in Figure 5.

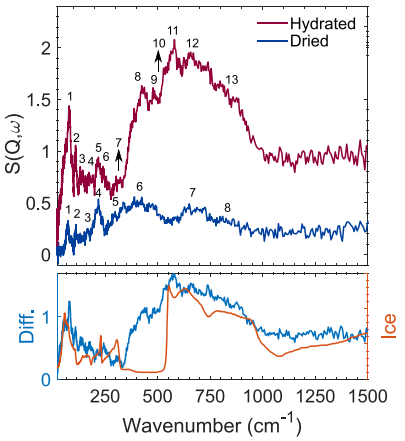

Figure 5. INS experimental spectra of Ni-Hec in dried (145 °C under vacuum) and hydrated states (equilibrated at 43% r.h.). The difference spectrum below is compared with the INS spectrum of ice Ih as a standard reference (in orange and scaled by the right axis). As a result of an ordered H-bond network, amorphous Ih is characterized by a pronounced librational edge. Numbers and arrows highlight important modes summarized in Tables S1 and S2. The spectra were recorded at $T < 20$ K.

Dried Ni-Hec before CO_2 Exposure. In the spectrum for the dried Ni-Hec sample (Figure 5), we observe peaks at 70, 109, 165, 215, and 300 cm^{-1} (#1, #2, #3, #4, and #5), a broad distribution centered around 400 cm^{-1} (#6), a broad distribution centered around 670 cm^{-1} (#7), and a broad shoulder centered at 810 cm^{-1} (#8). Previous INS measurements on β-$Ni(OH)_2$ have shown peaks at 90, 115, 294/313, 358, 394, 421/452, 680, and 880 cm^{-1}.[45,52] In agreement with the findings by Loch et al.,[24] where the structure was identified as $[Ni(OH)_{0.83}(H_2O)_{1.17}]_{0.37}^{1.17+}$, the sharp peaks at 70 and 215 cm^{-1} (#1, #4) are correlated with the confined water coordinated to the nickel hydroxide species.[53] One could question whether the peaks might be related to partial hydrolysis of Mg_3F-moieties giving rise to a structure Mg_3OH. This is, however, unlikely as the Ni-Hec was obtained by ion exchange of melt-synthesized Na-Hec (Figure S3), which lacks bands in this region. Modes and tentative assignment are summarized in Table S1.

Hydrated Ni-Hec before CO_2 Exposure. For hydrated Ni-Hec equilibrated at 43% r.h., corresponding to a 2 WL hydration as in the PXRD/Raman spectroscopy measurements (Figure 5), which contains both $[Ni(H_2O_6)]^{2+}$ and $[Ni(OH)_{0.83}(H_2O)_{1.17}]_{0.37}^{1.17+}$, we observe a sharp peak on a broad distribution at 76 cm^{-1} (#1), in addition to sharp peaks at 109, 215, and 237 cm^{-1} (#2, #5, and #6), and minor vibrations centered around 130 and 165 cm^{-1} (#3 and #4). From 335 to 1000 cm^{-1}, a broad distribution is found, with sharper features at 430, 480, 575, 650, and 800 cm^{-1} (#8, #9, #11, #12, and #13). The hydrated Ni-Hec shows the same modes as the dried sample associated to the Ni−OH moieties as well as new modes associated to water (see further discussion below). Modes and the assignment are summarized in Table S2.

In the difference spectrum in Figure 5, since we have removed the contribution from the clay and the condensed $[Ni(OH)_{0.83}(H_2O)_{1.17}]_{0.37}^{1.17+}$, we are left only with the contribution from different types of water present in this sample. Considering that INS is in particular sensitive to intramolecular water librational modes located between 300 and 1100 cm^{-1}, we can argue that the sharp librational edge at 336 cm^{-1}, previously observed in beidellite and montmorillonite[26] and shown to have a clear dependence on the interlayer cation, here originates from water coordinated to Ni^{2+}. The second onset around 510 cm^{-1} with a significant peak at 580 cm^{-1} suggests the presence of less confined interlayer water, which is the noncoordinated interlayer water and responsible for the water loss below 100 °C observed in the TGA data (Figure S6). The absence of a clear librational edge similar to ice confirms the absence of a significant amount of noninterlayer water. The presence of these assigned water populations is further confirmed by analyzing the low energy region of the spectra. Free bulk water[54] is characterized with an excitation around 50 cm^{-1}, while confined water molecules are characterized by a vibrational mode centered at about 80 cm^{-1}.[54,55] Thus, the observation of the sharp peak at 76 cm^{-1} is indicative of interlayer water coordinated to the Ni^{2+} cation, while the observation of a broad shoulder toward 50 cm^{-1}, also observed recently by Larsen et al.,[55] is consistent with the presence of water that is not coordinated with cations.

Dried Ni-Hec after CO_2 Exposure. Pronounced changes in the INS spectra are observed for the dried Ni-Hec (Figure 6a,b) upon CO_2 exposure. For the dried sample exposed to 5 bars of CO_2 at low energy transfer, a gain of intensity at 50 cm^{-1}, followed by an intensity loss at 72 cm^{-1}, and broad intensity gain between 80 and 160 cm^{-1} and at 176 cm^{-1} are observed. At 44 bar of CO_2, the signal in this region is more pronounced. Both at 5 and 44 bar, with the broad peaks centered around 215 and 400 cm^{-1}, a significant intensity loss was recorded. At 5 bar, there are still visible peaks left associated to the Ni−OH moieties at 336, 420, and 470 cm^{-1}, which are quite suppressed at 44 bar. Furthermore, at 5 bar, we observe an excess in energy at 675 cm^{-1} that transforms into a sharp peak at 655 cm^{-1} when increasing the CO_2 pressure to 44 bar.

For dried Ni-Hec after removing CO_2 by applying vacuum (Figure 6c), we observe at low wavenumbers a small increase of intensity at 50, 70, and 101 cm^{-1}, whereas at higher energy transfers, the broad peaks centered at 215 and 400 cm^{-1} have not reached their full initial prominence. The onset of the peak centered at 680 cm^{-1} has a shift to 530 cm^{-1} from 610 cm^{-1}. The signal seems to a large degree to return the initial signal, however, not to full prominence.

https://dx.doi.org/10.1021/acs.jpcc.0c07206
J. Phys. Chem. C 2020, 124, 26222−26231

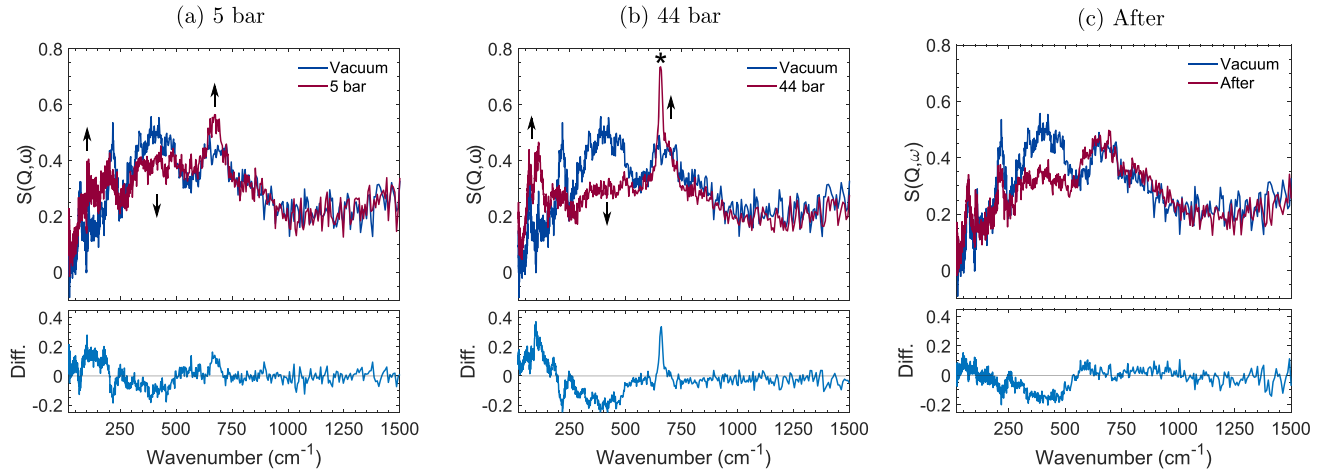

Figure 6. INS experimental spectra of the dried Ni-Hec initial state and that exposed to (a) 5 bar of CO_2, (b) 44 bar of CO_2 and (c) after cycling (loading and pumping) with the corresponding difference spectra given below. Loading of CO_2 was performed at room temperature, and the spectra were recorded at $T < 20$ K. Arrows and asterisk (*) highlight important changes in the spectra.

For dried Ni-Hec, the modes associated to the $[Ni(OH)_{0.83}(H_2O)_{1.17}]_{0.37}^{1.17+}$ interlayer species are severely attenuated (Figure 6b) and considerable crystalline swelling due to CO_2 exposure is observed (Figure 1). INS, gravimetric adsorption, and PXRD data on dried Na-Hec are presented in the Supporting Information, where neither uptake, swelling, nor spectroscopic changes are observed. As no changes are found when dried Na-Hec is exposed to CO_2 and, in addition, previous observations on cations with high hydration enthalpy[8,10,22] show no swelling, this suggest that the smectite-like interlayer does not play a role for the CO_2 capture in the dried case. Thus, the $[Ni(OH)_{0.83}(H_2O)_{1.17}]_{0.37}^{1.17+}$ species plays the important role in the adsorption of CO_2 by dried Ni-Hec. This then means that the smectite layers remain unchanged with a d-spacing of about 10 Å and that the chlorite-like layers swell from about 13−14 to 15−16 Å. This reaction must be reversible since our PXRD experiments with repeated exposure to CO_2, a long (>24 h) evacuation of the sample or moderate heating (>50 °C) is sufficient to return the Bragg reflection to the same initial position. This suggests that the observed state by INS after releasing the CO_2 (Figure 6c) is a transient step during the return to the initial structure and that there is still some CO_2 adsorbed to the structure. However, based on the present data, we cannot completely rule out the possibility that the reaction between CO_2 and nickel hydroxide contained within the clay produces permanent structural changes to nickel hydroxide islands.

Hydrated Ni-Hec after CO_2 Exposure. After being exposed to CO_2 at room temperature and cooled down to $T < 20$ K, for the hydrated Ni-Hec (Figure 7), the changes are evident in the difference spectrum, and new modes are observed at 64, 95, and 117 cm^{-1}. There is also a slight increase of intensity around 315 cm^{-1} and a small general loss of intensity between 400 and 900 cm^{-1}. In addition, a new vibration is observed at 655 cm^{-1}.

As various different hydrogenated species (coordinated and non-coordinated interlayer water, and $[Ni(OH)_{0.83}(H_2O)_{1.17}]_{0.37}^{1.17+}$) coexist for hydrated Ni-Hec, it is less obvious whether the changes observed by INS upon CO_2 exposure are a consequence of changes in the librational modes associated to one or more of the water species or by direct

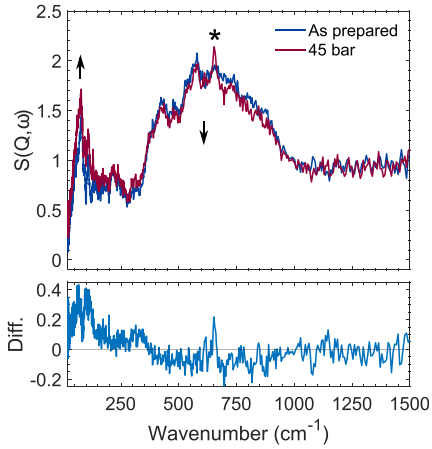

Figure 7. INS experimental spectra of hydrated Ni-Hec (equilibrated 43% r.h.) in the initial state and exposed to 44 bar of CO_2 at room temperature. Arrows and asterisk (*) highlight important changes in the spectra. The spectra were recorded at $T < 20$ K.

association to the $[Ni(OH)_{0.83}(H_2O)_{1.17}]_{0.37}^{1.17+}$. The negligible changes along the librational edge agree with a strong coordination of water with Ni^{2+}, which is not disrupted by CO_2 exposure. However, we observe changes in the modes of the interlayer water by Raman spectroscopy (Figure 4), which together with the INS observations may be indicative of influence on the non-coordinated interlayer water by CO_2. The general loss of INS intensity, similar to the dried case, suggests a similar interaction between CO_2 and interlayer $[Ni(OH)_{0.83}(H_2O)_{1.17}]_{0.37}^{1.17+}$ both for dried and hydrated Ni-Hec. In addition, by Raman spectroscopy, we observe clear changes in what we identify as the OH-stretching modes of the intercalated nickel hydroxide, indicating an interaction with CO_2. The smaller crystalline swelling of hydrated Ni-Hec compared to the dried case (Figure 2) is due to the layers being more similar to one another for hydrated Ni-Hec. We can assume that the smectite-like interlayer remains unchanged at about 15 Å, which is evidenced by the observed stability of the H-bonding by INS. Then, the chlorite-like layer swells from about 14−15 Å, and the chlorite-like layer could adopt a similar structure to what is observed for the dried state. The observed improved ordering is similar to what has previously

https://dx.doi.org/10.1021/acs.jpcc.0c07206
J. Phys. Chem. C 2020, 124, 26222−26231

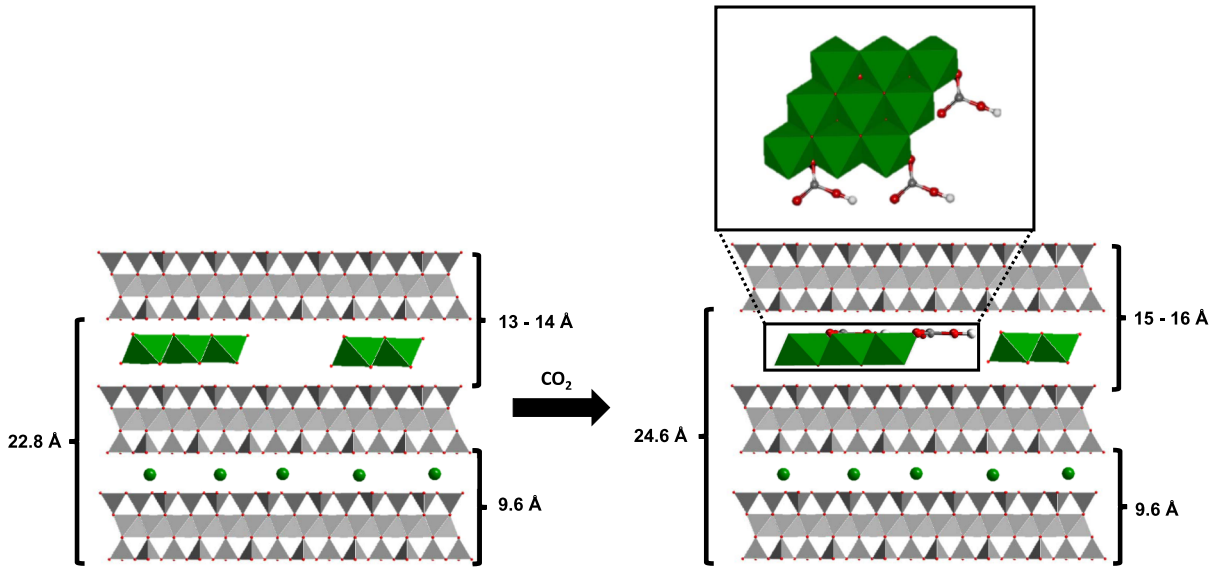

Figure 8. Hypothesized model for crystalline swelling in Ni-Hec clay in response to CO_2 exposure. The CO_2 interacts only with and causes swelling only of chlorite-like layers.

been observed upon hydration of Na-Hec and[4] suggests that the incorporation of CO_2 in the interlayer strengthens the interaction between the interlayer species and 2:1 clay layers.

Further Discussion. For both the dried and the hydrated sample, a peak is forming at 655 cm^{-1}, (marked by an asterisk in Figure 6b), accompanied with vibrations at 64, 95, and 117 cm^{-1}. For the vibration at 655 cm^{-1}, we may suggest three possibilities based on the literature: Librational modes for water are observed in this region, bending modes for CO_2 are also observed at 640 cm^{-1}[56] as well as modes associated to bicarbonates.[57] As this peak is not observed in the spectra of the dried Na-Hec (see Supporting Information), formation of solid CO_2 on the external surfaces of the Hec samples or in the remaining probing volume of the neutrons in the sample cell is unlikely. Notably the cross section of CO_2 is 20 times lower than that of hydrogen; thus, the observation of this peak is unlikely to be due to the bending mode of CO_2. It is possible that these changes also are associated with local changes of the water population. Following this reasoning, the peak that gains intensity at 64 cm^{-1} could suggest a more ordered water population.[54] The sharp vibration at 655 cm^{-1} could also originate from a specific librational mode associated to this ordered water state, possibly through segregation of some water molecules to monomers and dimers.[58] Water confinement in UO_2F_2 displays a peak at 778 cm^{-1}, that simulations attribute to a librational phonon mode along the a/b-axis at 712 cm^{-1}, due to confined water within the van der Waals gap of that material.[59] The incorporation of CO_2 in the interlayer may then force some of the H_2O associated with the hydroxide species into a more confined situation. If we consider that the hydrogen bonds in HCO_3^- are weak, we may assign the present INS modes to HCO_3^- based on the study of Fillaux et al. on potassium bicarbonate.[57] However, there are no observed bicarbonate modes by Raman spectroscopy (Figure 4).

From the current experiments, it still is unclear what is the reaction between CO_2 and the $[Ni(OH)_{0.83}(H_2O)_{1.17}]_{0.37}^{1.17+}$ species. A possible mechanism that can be suggested has been observed on goethite under anhydrous conditions,[60] where CO_2 is chemisorbed according to Ni−OH + CO_2 → Ni−O-(HCO_2). By this reaction, hydroxide groups are converted into bicarbonate and this would significantly reduce the intensity associated to the corresponding modes. The chemisorbed CO_2 may then be grafted as a bicarbonate to the condensed nickel hydroxide species, causing the swelling by adopting a structure as illustrated in Figure 8. However, as no bicarbonate modes are unambiguously observed by Raman spectroscopy, this is not evident from the present data.

Nevertheless, our experimental data show clear evidence that the intercalated $[Ni(OH)_{0.83}(H_2O)_{1.17}]_{0.37}^{1.17+}$ species play a crucial role in the incorporation of CO_2 in the interlayers, both for the dried and hydrated cases. This is corroborated by DFT simulations (Figure 9), which are consistent with the

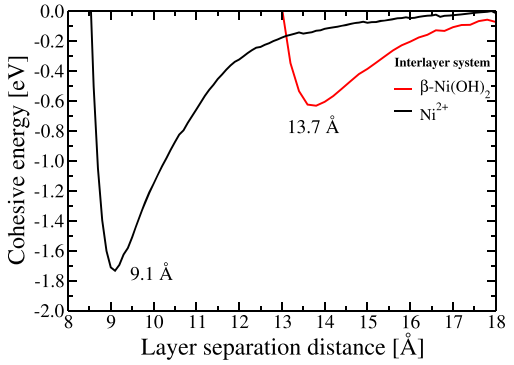

Figure 9. Basal spacing and energy per unit cell cohesive energy obtained by computational studies based on DFT calculations for the dehydrated smectite layers with Ni^{2+} and chlorite-like layers with a confined β-$Ni(OH)_2$.

experimentally observed *d*-spacing of the dehydrated system here and in the study by Loch et al.[24] In addition, the simulations (Figure 9) show that the cohesion energy of the chlorite-like layers (−0.63 eV) is significantly lower than that for the smectite-like layers (−1.73 eV). This strengthens our arguments that the chlorite-like layers are responsible for the CO_2 uptake and swelling in this system. Based on these calculations, we can argue that CO_2 in the chlorite-like layers may attach to the edge of the nickel hydroxide islands and bind

https://dx.doi.org/10.1021/acs.jpcc.0c07206
J. Phys. Chem. C 2020, 124, 26222−26231

to not fully coordinated nickel atoms forming a strong bond (E_{Ads}), see Supporting Information.

CONCLUSIONS

Developing new sorbent materials for CO_2 is of key importance to solve issues related to greenhouse gas emissions. By PXRD, Raman spectroscopy, and INS, we identified a hitherto overlooked mechanism for CO_2 adsorption in hectorite clay. With these techniques, we took a new approach, where we study the mechanism for CO_2 adsorption from the perspective of interlayer hydrogeneous species, that is hydroxides and water. Phase pure and charge homogeneous synthetic fluorohectorite provides a unique template for studying such interactions as it has no structural hydrogen incorporated in the 2:1 clay layer structure. For Ni-exchanged hectorite, an ordered interstratification of chlorite-like layers and smectite-like layers, we found that the intercalated nickel hydroxide promotes incorporation of CO_2 in the clay interlayers. Our results suggest that the CO_2 binds to the $[Ni(OH)_{0.83}(H_2O)_{1.17}]_{0.37}^{1.17+}$ species, both in the dried and the hydrated case, and is responsible for swelling in response to CO_2. No incorporation of CO_2 was found in the smectite-like layers for the dried case. Furthermore, CO_2 has limited impact on the water coordinated to the interlayer cations for the hydrated case.

In future work, we will perform ion exchange with a variety of transition metal elements known for their condensation tendency at slightly elevated pH (>8). As shown in the literature,[61−63] this will produce condensed chlorite-type interlayers only and therefore should increase the adsorption capacity for CO_2, rendering Ni-exchanged hectorite technologically competitive to other adsorption materials.

ASSOCIATED CONTENT

Supporting Information

The Supporting Information is available free of charge at https://pubs.acs.org/doi/10.1021/acs.jpcc.0c07206.

> Supporting INS and PXRDmeasurements of dried Na-Hec; diffractograms of hydrated Ni-Hec; gravimetric adsorption measurements on Ni-Hec and Na-Hec; thermogravimetric analysis of Ni-Hec and Na-Hec; and tables of assigned modes for INS (PDF)

AUTHOR INFORMATION

Corresponding Authors

Josef Breu − *Bavarian Polymer Institute and Department of Chemistry, University of Bayreuth, D-95440 Bayreuth, Germany;* orcid.org/0000-0002-2547-3950; Phone: +49 (0)921 / 55-2530; Email: josef.breu@uni-bayreuth.de

Heloisa N. Bordallo − *Niels Bohr Institute-University of Copenhagen, 2100 Copenhagen, Denmark; European Spallation Source ESS ERIC, SE-221 00 Lund, Sweden;* orcid.org/0000-0003-0750-0553; Phone: +45 21 30 88 29; Email: bordallo@nbi.ku.dk

Jon Otto Fossum − *Department of Physics, Norwegian University of Science and Technology, 7491 Trondheim, Norway;* orcid.org/0000-0002-8952-303X; Phone: +47 911 39 194; Email: jon.fossum@ntnu.no

Authors

Kristoffer W. Bø Hunvik − *Department of Physics, Norwegian University of Science and Technology, 7491 Trondheim, Norway*

Patrick Loch − *Bavarian Polymer Institute and Department of Chemistry, University of Bayreuth, D-95440 Bayreuth, Germany*

Leide P. Cavalcanti − *Institute for Energy Technology (IFE), N-2027 Kjeller, Norway; ISIS Neutron and Muon Source, STFC Rutherford Appleton Laboratory, OX11 0QX Didcot, U.K.;* orcid.org/0000-0002-0408-0058

Konstanse Kvalem Seljelid − *Department of Physics, Norwegian University of Science and Technology, 7491 Trondheim, Norway*

Paul Monceyron Røren − *Department of Physics, Norwegian University of Science and Technology, 7491 Trondheim, Norway*

Svemir Rudić − *ISIS Neutron and Muon Source, STFC Rutherford Appleton Laboratory, OX11 0QX Didcot, U.K.*

Dirk Wallacher − *Department Sample Environments, Helmholtz-Zentrum Berlin für Materialien und Energie, 14109 Berlin, Germany*

Alexsandro Kirch − *Departamento de Física dos Materiais e Mecânica, Instituto de Física, Universidade de São Paulo, 05508-090 São Paulo, São Paulo, Brazil*

Kenneth Dahl Knudsen − *Institute for Energy Technology (IFE), N-2027 Kjeller, Norway; Department of Physics, Norwegian University of Science and Technology, 7491 Trondheim, Norway*

Caetano Rodrigues Miranda − *Departamento de Física dos Materiais e Mecânica, Instituto de Física, Universidade de São Paulo, 05508-090 São Paulo, São Paulo, Brazil*

Complete contact information is available at: https://pubs.acs.org/10.1021/acs.jpcc.0c07206

Notes

The authors declare no competing financial interest.

ACKNOWLEDGMENTS

This work was supported by the Research Council of Norway under the Frinatek Program, project number 250728. This work was supported by the Deutsche Forschungsgemeinschaft (SFB 840). P.L. thanks Elite Network Bavaria in the framework of the Elite Study Program "Macromolecular Science" for support. A.K. and C.R.M. gratefully acknowledge the Research Centre for Gas Innovation (RCGI) and support from the Brazilian agencies FAPESP (2017/02317−2) and CNPq. We acknowledge the European Synchrotron Radiation Facility for provision of synchrotron radiation facilities and we would like to thank Wouter van Beek, Vadim Diadkin, and Dmitry Chernyshov for excellent assistance in using beamline SNBL BM01. Experiments at the ISIS Pulsed Neutron and Muon Source were supported by a beamtime allocation from the Science and Technology Facilities Council.[64] Paulo Henrique Michels-Brito, Koiti Araki, and Leander Michels are acknowledged for helpful discussions.

REFERENCES

(1) Bergaya, F.; Lagaly, G. *Handbook of clay science*; Newnes, 2013.
(2) Daab, M.; Eichstaedt, N. J.; Habel, C.; Rosenfeldt, S.; Kalo, H.; Schießling, H.; Förster, S.; Breu, J. Onset of Osmotic Swelling in Highly Charged Clay Minerals. *Langmuir* **2018**, *34*, 8215−8222.

(3) Dazas, B.; Lanson, B.; Breu, J.; Robert, J.-L.; Pelletier, M.; Ferrage, E. Smectite fluorination and its impact on interlayer water content and structure: A way to fine tune the hydrophilicity of clay surfaces? *Microporous Mesoporous Mater.* **2013**, *181*, 233−247.
(4) Kalo, H.; Milius, W.; Breu, J. Single crystal structure refinement of one- and two-layer hydrates of sodium fluorohectorite. *RSC Adv.* **2012**, *2*, 8452−8459.
(5) Hemmen, H.; Rolseth, E. G.; Fonseca, D. M.; Hansen, E. L.; Fossum, J. O.; Plivelic, T. S. X-ray studies of carbon dioxide intercalation in Na-fluorohectorite clay at near-ambient conditions. *Langmuir* **2012**, *28*, 1678−1682.
(6) Michels, L.; Fossum, J. O.; Rozynek, Z.; Hemmen, H.; Rustenberg, K.; Sobas, P. A.; Kalantzopoulos, G. N.; Knudsen, K. D.; Janek, M.; Plivelic, T. S.; et al. Intercalation and retention of carbon dioxide in a smectite clay promoted by interlayer cations. *Sci. Rep.* **2015**, *5*, 8775.
(7) Cavalcanti, L. P.; Kalantzopoulos, G. N.; Eckert, J.; Knudsen, K. D.; Fossum, J. O. A nano-silicate material with exceptional capacity for CO 2 capture and storage at room temperature. *Sci. Rep.* **2018**, *8*, 11827.
(8) Schaef, H. T.; Loganathan, N.; Bowers, G. M.; Kirkpatrick, R. J.; Yazaydin, A. O.; Burton, S. D.; Hoyt, D. W.; Thanthiriwatte, K. S.; Dixon, D. A.; McGrail, B. P.; et al. Tipping point for expansion of layered aluminosilicates in weakly polar solvents: supercritical CO2. *ACS Appl. Mater. Interfaces* **2017**, *9*, 36783−36791.
(9) Loganathan, N.; Bowers, G. M.; Yazaydin, A. O.; Schaef, H. T.; Loring, J. S.; Kalinichev, A. G.; Kirkpatrick, R. J. Clay swelling in dry supercritical carbon dioxide: effects of interlayer cations on the structure, dynamics, and energetics of CO2 intercalation probed by XRD, NMR, and GCMD simulations. *J. Phys. Chem. C* **2018**, *122*, 4391−4402.
(10) Loganathan, N.; Bowers, G. M.; Yazaydin, A. O.; Kalinichev, A. G.; Kirkpatrick, R. J. Competitive Adsorption of H2O and CO2 in 2-Dimensional Nanoconfinement: GCMD Simulations of Cs-and Ca-Hectorites. *J. Phys. Chem. C* **2018**, *122*, 23460−23469.
(11) dos Santos, E. C.; Gates, W. P.; Michels, L.; Juranyi, F.; Mikkelsen, A.; da Silva, G. J.; Fossum, J. O.; Bordallo, H. N. The pH influence on the intercalation of the bioactive agent ciprofloxacin in fluorohectorite. *Appl. Clay Sci.* **2018**, *166*, 288−298.
(12) Herling, M. M.; Rieß, M.; Sato, H.; Li, L.; Martin, T.; Kalo, H.; Matsuda, R.; Kitagawa, S.; Breu, J. Purely Physisorption-Based CO-Selective Gate-Opening in Microporous Organically Pillared Layered Silicates. *Angew. Chem.* **2018**, *130*, 573−577.
(13) Schaef, H. T.; Ilton, E. S.; Qafoku, O.; Martin, P. F.; Felmy, A. R.; Rosso, K. M. In situ XRD study of Ca2+ saturated montmorillonite (STX-1) exposed to anhydrous and wet supercritical carbon dioxide. *Int. J. Greenhouse Gas Control* **2012**, *6*, 220−229.
(14) Schaef, H. T.; Loring, J. S.; Glezakou, V.-A.; Miller, Q. R. S.; Chen, J.; Owen, A. T.; Lee, M.-S.; Ilton, E. S.; Felmy, A. R.; McGrail, B. P.; et al. Competitive sorption of CO2 and H2O in 2: 1 layer phyllosilicates. *Geochim. Cosmochim. Acta* **2015**, *161*, 248−257.
(15) Loring, J. S.; Schaef, H. T.; Turcu, R. V. F.; Thompson, C. J.; Miller, Q. R. S.; Martin, P. F.; Hu, J.; Hoyt, D. W.; Qafoku, O.; Ilton, E. S.; et al. In situ molecular spectroscopic evidence for CO2 intercalation into montmorillonite in supercritical carbon dioxide. *Langmuir* **2012**, *28*, 7125−7128.
(16) Loring, J. S.; Ilton, E. S.; Chen, J.; Thompson, C. J.; Martin, P. F.; Bénézeth, P.; Rosso, K. M.; Felmy, A. R.; Schaef, H. T. In situ study of CO2 and H2O partitioning between Na−montmorillonite and variably wet supercritical carbon dioxide. *Langmuir* **2014**, *30*, 6120−6128.
(17) Loring, J. S.; Schaef, H. T.; Thompson, C. J.; Turcu, R. V.; Miller, Q. R.; Chen, J.; Hu, J.; Hoyt, D. W.; Martin, P. F.; Ilton, E. S.; et al. Clay hydration/dehydration in dry to water-saturated supercritical CO2: implications for caprock integrity. *Energy Procedia* **2013**, *37*, 5443−5448.
(18) Giesting, P.; Guggenheim, S.; Koster van Groos, A. F.; Busch, A. Interaction of carbon dioxide with Na-exchanged montmorillonite at pressures to 640 bars: Implications for CO2 sequestration. *Int. J. Greenhouse Gas Control* **2012**, *8*, 73−81.
(19) Hwang, J.; Joss, L.; Pini, R. Measuring and modelling supercritical adsorption of CO2 and CH4 on montmorillonite source clay. *Microporous Mesoporous Mater.* **2019**, *273*, 107−121.
(20) Rother, G.; Ilton, E. S.; Wallacher, D.; Hauβ, T.; Schaef, H. T.; Qafoku, O.; Rosso, K. M.; Felmy, A. R.; Krukowski, E. G.; Stack, A. G.; et al. CO2 sorption to subsingle hydration layer montmorillonite clay studied by excess sorption and neutron diffraction measurements. *Environ. Sci. Technol.* **2013**, *47*, 205−211.
(21) Botan, A.; Rotenberg, B.; Marry, V.; Turq, P.; Noetinger, B. Carbon dioxide in montmorillonite clay hydrates: thermodynamics, structure, and transport from molecular simulation. *J. Phys. Chem. C* **2010**, *114*, 14962−14969.
(22) Loganathan, N.; Yazaydin, A. O.; Kirkpatrick, R. J.; Bowers, G. M. Tuning the Hydrophobicity of Layer-Structure Silicates To Promote Adsorption of Nonaqueous Fluids: Effects of F−for OH− Substitution on CO2 Partitioning into Smectite Interlayers. *J. Phys. Chem. C* **2019**, *123*, 4848−4855.
(23) Altoé, M. A. S.; Michels, L.; Santos, E. C. d.; Droppa, R., Jr; Grassi, G.; Ribeiro, L.; Knudsen, K. D.; Bordallo, H. N.; Fossum, J. O.; da Silva, G. J. Continuous water adsorption states promoted by Ni2+ confined in a synthetic smectite. *Appl. Clay Sci.* **2016**, *123*, 83−91.
(24) Loch, P.; Hunvik, K. W. B.; Puchtler, F.; Weiß, S.; Seljelid, K. K.; Røren, P. M.; Rudic, S.; Raaen, S.; Knudsen, K. D.; Bordallo, H. N.; et al. Spontaneous formation of an ordered interstratification upon Ni-exchange of Na-fluorohectorite. *Appl. Clay Sci.* **2020**, *198*, 105831.
(25) Martins, M. L.; Gates, W. P.; Michot, L.; Ferrage, E.; Marry, V.; Bordallo, H. N. Neutron scattering, a powerful tool to study clay minerals. *Appl. Clay Sci.* **2014**, *96*, 22−35.
(26) Cygan, R. T.; Daemen, L. L.; Ilgen, A. G.; Krumhansl, J. L.; Nenoff, T. M. Inelastic neutron scattering and molecular simulation of the dynamics of interlayer water in smectite clay minerals. *J. Phys. Chem. C* **2015**, *119*, 28005−28019.
(27) Jiménez-Ruiz, M.; Ferrage, E.; Blanchard, M.; Fernandez-Castanon, J.; Delville, A.; Johnson, M. R.; Michot, L. J. Combination of inelastic neutron scattering experiments and ab Initio quantum calculations for the study of the hydration properties of oriented Saponites. *J. Phys. Chem. C* **2017**, *121*, 5029−5040.
(28) Stöter, M.; Kunz, D. A.; Schmidt, M.; Hirsemann, D.; Kalo, H.; Putz, B.; Senker, J.; Breu, J. Nanoplatelets of sodium hectorite showing aspect ratios of 20 000 and superior purity. *Langmuir* **2013**, *29*, 1280−1285.
(29) Dyadkin, V.; Pattison, P.; Dmitriev, V.; Chernyshov, D. A new multipurpose diffractometer PILATUS@ SNBL. *J. Synchrotron Radiat.* **2016**, *23*, 825−829.
(30) Jensen, T. R.; Nielsen, T. K.; Filinchuk, Y.; Jørgensen, J.-E.; Cerenius, Y.; Gray, E. M.; Webb, C. J. Versatile in situ powder X-ray diffraction cells for solid−gas investigations. *J. Appl. Crystallogr.* **2010**, *43*, 1456−1463.
(31) Pinna, R. S.; Rudić, S.; Parker, S. F.; Armstrong, J.; Zanetti, M.; Škoro, G.; Waller, S. P.; Zacek, D.; Smith, C. A.; Capstick, M. J.; et al. The neutron guide upgrade of the TOSCA spectrometer. *Nucl. Instrum. Methods Phys. Res. Sect. A Accel. Spectrom. Detect. Assoc. Equip.* **2018**, *896*, 68−74.
(32) Parker, S. F.; Fernandez-Alonso, F.; Ramirez-Cuesta, A. J.; Tomkinson, J.; Rudic, S.; Pinna, R. S.; Gorini, G.; Fernández Castañon, J. Recent and future developments on TOSCA at ISIS. *J. Phys.: Conf. Ser.* **2014**, *554*, 012003.
(33) Mitchell, P. C. H. *Vibrational Spectroscopy with Neutrons: with Applications in Chemistry, Biology, Materials Science and Catalysis*; World Scientific, 2005; Vol. 3.
(34) Arnold, O.; Bilheux, J. C.; Borreguero, J. M.; Buts, A.; Campbell, S. I.; Chapon, L.; Doucet, M.; Draper, N.; Ferraz Leal, R.; Gigg, M. A.; et al. Mantid—Data analysis and visualization package for neutron scattering and μ SR experiments. *Nucl. Instrum. Methods Phys. Res. Sect. A Accel. Spectrom. Detect. Assoc. Equip.* **2014**, *764*, 156−166.

https://dx.doi.org/10.1021/acs.jpcc.0c07206
J. Phys. Chem. C 2020, 124, 26222−26231

(35) Hohenberg, P.; Kohn, W. Inhomogeneous electron gas. *Phys. Rev.* **1964**, *136*, B864.
(36) Kohn, W.; Sham, L. J. Self-consistent equations including exchange and correlation effects. *Phys. Rev.* **1965**, *140*, A1133.
(37) Berland, K.; Hyldgaard, P. Exchange functional that tests the robustness of the plasmon description of the van der Waals density functional. *Phys. Rev. B: Condens. Matter Mater. Phys.* **2014**, *89*, 035412.
(38) Soler, J. M.; Artacho, E.; Gale, J. D.; García, A.; Junquera, J.; Ordejón, P.; Sánchez-Portal, D. The SIESTA method for ab initio order-N materials simulation. *J. Phys.: Condens. Matter* **2002**, *14*, 2745.
(39) Breu, J.; Seidl, W.; Stoll, A. Fehlordnung bei smectiten in abhängigkeit vom zwischenschichtkation. *Z. Anorg. Allg. Chem.* **2003**, *629*, 503−515.
(40) Curtarolo, S.; Setyawan, W.; Wang, S.; Xue, J.; Yang, K.; Taylor, R. H.; Nelson, L. J.; Hart, G. L. W.; Sanvito, S.; Buongiorno-Nardelli, M.; et al. AFLOWLIB.ORG: A distributed materials properties repository from high-throughput ab initio calculations. *Comput. Mater. Sci.* **2012**, *58*, 227−235.
(41) Busch, A.; Bertier, P.; Gensterblum, Y.; Rother, G.; Spiers, C. J.; Zhang, M.; Wentinck, H. M. On sorption and swelling of CO2 in clays. *Geomech. Geophys. Geo-Energy Geo-Resour.* **2016**, *2*, 111−130.
(42) Kloprogge, J. *Developments in Clay Science*; Elsevier, 2017; Vol. *8*; pp 150−199.
(43) Hall, D. S.; Lockwood, D. J.; Poirier, S.; Bock, C.; MacDougall, B. R. Raman and infrared spectroscopy of α and β phases of thin nickel hydroxide films electrochemically formed on nickel. *J. Phys. Chem. A* **2012**, *116*, 6771−6784.
(44) Rinaudo, C.; Roz, M.; Boero, V.; Franchini-Angela, M. FT-Raman spectroscopy on several di-and trioctahedral T−O−T phyllosilicates. *Neues Jahrbuch Mineral. Monatsh.* **2004**, *2004*, 537−554.
(45) Bantignies, J. L.; Deabate, S.; Righi, A.; Rols, S.; Hermet, P.; Sauvajol, J. L.; Henn, F. New insight into the vibrational behavior of nickel hydroxide and oxyhydroxide using inelastic neutron scattering, far/mid-infrared and Raman spectroscopies. *J. Phys. Chem. C* **2008**, *112*, 2193−2201.
(46) Gates, W. P.; Bordallo, H. N.; Aldridge, L. P.; Seydel, T.; Jacobsen, H.; Marry, V.; Churchman, G. J. Neutron time-of-flight quantification of water desorption isotherms of montmorillonite. *J. Phys. Chem. C* **2012**, *116*, 5558−5570.
(47) Frost, R. L.; Rintoul, L. Lattice vibrations of montmorillonite: an FT Raman and X-ray diffraction study. *Appl. Clay Sci.* **1996**, *11*, 171−183.
(48) Hall, D. S.; Lockwood, D. J.; Poirier, S.; Bock, C.; MacDougall, B. R. Applications of in situ Raman spectroscopy for identifying nickel hydroxide materials and surface layers during chemical aging. *ACS Appl. Mater. Interfaces* **2014**, *6*, 3141−3149.
(49) Frost, R. L.; Dickfos, M. J.; Jagannadha Reddy, B. Raman spectroscopy of hydroxy nickel carbonate minerals nullaginite and zaratite. *J. Raman Spectrosc.* **2008**, *39*, 1250−1256.
(50) Arab, M.; Bougeard, D.; Smirnov, K. S. Experimental and computer simulation study of the vibrational spectra of vermiculite. *Phys. Chem. Chem. Phys.* **2002**, *4*, 1957−1963.
(51) Anderson, G. R. The Raman spectra of carbon dioxide in liquid water and water-d2. *J. Phys. Chem.* **1977**, *81*, 273−276.
(52) Baddour-Hadjean, R.; Fillaux, F.; Tomkinson, J. Proton dynamics in βNi (OH) 2 and βNiOOH. *Phys. B* **1995**, *213−214*, 637−639.
(53) Persson, R. A. X.; Pattni, V.; Singh, A.; Kast, S. M.; Heyden, M. Signatures of solvation thermodynamics in spectra of intermolecular vibrations. *J. Chem. Theory Comput.* **2017**, *13*, 4467−4481.
(54) Berg, M. C.; Dalby, K. N.; Tsapatsaris, N.; Okhrimenko, D. V.; Sørensen, H. O.; Jha, D.; Embs, J. P.; Stipp, S. L. S.; Bordallo, H. N. Water Mobility in Chalk: A Quasielastic Neutron Scattering Study. *J. Phys. Chem. C* **2017**, *121*, 14088−14095.
(55) Larsen, S. R.; Michels, L.; dos Santos, É. C.; Berg, M. C.; Gates, W. P.; Aldridge, L. P.; Seydel, T.; Ollivier, J.; Telling, M. T. F.; Fossum, J. O.; et al. Physicochemical characterisation of fluorohectorite: Water dynamics and nanocarrier properties. *Microporous Mesoporous Mater.* **2020**, *306*, 110512.
(56) Bandosz, T. J.; Seredych, M.; Rodríguez-Castellón, E.; Cheng, Y.; Daemen, L. L.; Ramírez-Cuesta, A. J. Evidence for CO2 reactive adsorption on nanoporous S-and N-doped carbon at ambient conditions. *Carbon* **2016**, *96*, 856−863.
(57) Fillaux, F.; Tomkinson, J.; Penfold, J. Proton dynamics in the hydrogen bond. The inelastic neutron scattering spectrum of potassium hydrogen carbonate at 5 K. *Chem. Phys.* **1988**, *124*, 425−437.
(58) Öberg, K. I.; Fraser, H. J.; Boogert, A. C. A.; Bisschop, S. E.; Fuchs, G. W.; van Dishoeck, E. F.; Linnartz, H. Effects of CO2 on H2O band profiles and band strengths in mixed H2O: CO2 ices. *Astron. Astrophys.* **2007**, *462*, 1187−1198.
(59) Miskowiec, A.; Niedziela, J. L.; Kirkegaard, M. C.; Shields, A. E. Analysis of Water Coupling in Inelastic Neutron Spectra of Uranyl Fluoride. *Sci. Rep.* **2019**, *9*, 10476.
(60) Yeşilbaş, M.; Song, X.; Boily, J.-F. Carbon Dioxide Binding in Supercooled Water Nanofilms on Nanominerals. *Environ. Sci.: Nano* **2020**, *7*, 437.
(61) Ohtsuka, K.; Suda, M.; Tsunoda, M.; Ono, M. Synthesis of metal hydroxide-layer silicate intercalation compounds (metal= Mg (II), Ca (II), Mn (II), Fe (II), Co (II), Ni (II), Zn (II), and Cd (II)). *Chem. Mater.* **1990**, *2*, 511−517.
(62) Uehara, M.; Yamzaki, A.; Umezawa, T.; Takahashi, K.; Tsutsumi, S. A nickel hydroxide-vermiculite complex: Preparation and characterization. *Clays Clay Miner.* **1999**, *47*, 726−731.
(63) Yamanaka, S.; Brindley, G. Hydroxy-nickel interlayering in montmorillonite by titration method. *Clays Clay Miner.* **1978**, *26*, 21−24.
(64) Fossum, J. O.; Knudsen, K. D.; Rudic, S.; Hunvik, K. W. B.; Bordallo, H. N.; Røren, P. M., *Determining the Interaction between Water and Carbon Dioxide in Smectite Clay (INS)*; STFC ISIS Neutron and Muon Source, 2019.

https://dx.doi.org/10.1021/acs.jpcc.0c07206
J. Phys. Chem. C 2020, 124, 26222−26231